Available online at www.sciencedirect.com
SCIENCE DIRECT®
Journal of Molecular Spectroscopy 221 (2003) 227–238
Journal of MOLECULAR SPECTROSCOPY
www.elsevier.com/locate/jms

Observation of bands among the four lowest pseudorotational states of 1,3-dioxolane

Dmitry G. Melnik,[a] Terry A. Miller,[a,*] and Frank C. De Lucia[b]

[a] *Department of Chemistry, The Ohio State University, 120 W. 18th Avenue, Columbus, OH 43210, USA*
[b] *Department of Physics, 174 W. 18th Avenue, Columbus, OH 43210, USA*

Received 28 April 2003; in revised form 14 July 2003

Abstract

The rotational transitions belonging to the pseudorotational bands $n = 0 \rightarrow 1$, $n = 2 \rightarrow 3$, and $n = 0 \rightarrow 3$ have been experimentally observed for 1,3-dioxolane in the spectral region of 153–364 GHz in a supersonic jet environment using the FASSST absorption spectrometer. Based on these observations, the symmetry ordering and the energy spacings of the four lowest states, $n = 0, 1, 2, 3$, have been established. The totality of the available data on this molecule, including those available from previously reported microwave studies has been analyzed, and a set of molecular constants has been obtained. Using the newly determined frequencies of the pseudorotational bands, along with the frequencies of the previously reported pseudorotational bands in the IR spectrum region, an empirical potential surface of 1,3-dioxolane has been obtained. The results of this analysis are compared to the potential surface and rotational constants obtained from quantum chemistry calculations.

1. Introduction

Small cyclic hydrocarbons (or substituted hydrocarbons) have idealized geometries corresponding to the simplest, planar geometric figures, e.g., triangles, squares, pentagons, hexagons, etc. Such idealized geometries are subject to distortion due to the necessity of achieving the maximum chemical bonding in the ground electronic state. For molecules satisfying the Jahn–Teller theorem, in-plane distortion is expected [1] and has been recently documented [2–4] in the aromatic (or nearly aromatic) C_5H_5, $C_6H_6^+$, and C_7H_7 radicals. For non-aromatic closed-shell cyclic hydrocarbons, out-of-plane distortions are expected to be most important. These distortions and the resulting potential energy surfaces (PES) are well discussed by Laane [5]. For four-membered rings, or other molecules with one ring puckering degree of freedom, the PES is well represented by a one-dimensional function, similarly, five-membered rings require a two-dimensional PES, six-membered rings a three-dimensional PES, and so on [6].

For the five-membered rings or the $e \times E$ Jahn–Teller active molecule, the vibrational or vibronic problem can be thought of in terms of a pseudorotational PES. Hindered pseudorotation (PR) of a five-membered ring, non-aromatic molecule results from the interaction of two degenerate or nearly degenerate out-of-plane ring puckering modes in the presence of a barrier to planarity in the molecule [7]. The obvious prototype of this kind of the molecular system is cyclopentane. However, as Pickett and Strauss showed [8], even considering the high symmetry of cyclopentane, some transitions between the PR levels are allowed in this molecule. Nevertheless, an extensive search in the region where the allowed PR bands have been predicted, produced no results [9], presumably, due to a small value of the transition moment. The first direct spectroscopic observation of the PR motion, was therefore made in tetrahydrofuran (THF) in low resolution IR experiments [10,11]. Later, the rotational spectra of THF in different PR states, as well as a few rotationally resolved tunneling bands, were obtained in microwave studies [12,13]. Recently, we have directly observed a PR band

* Corresponding author. Fax: 1-614-292-1948.
E-mail addresses: tamiller+@osu.edu (T.A. Miller), fcd@mps.ohio-state.edu (F.C. De Lucia).

0022-2852/$ - see front matter © 2003 Elsevier Inc. All rights reserved.
doi:10.1016/S0022-2852(03)00223-6

in the submillimeter wave region [14], which allowed a complete determination of the energy level pattern of the four lowest PR states. A combination of empirical and computational approaches in the study of THF allowed us to relate the symmetry properties of the lowest PR states with the shape of the potential surface for pseudorotation, and qualitatively explain the variations of the rotational constants in these states.

Although the study of THF enjoyed a certain success, it also made clear the desirability of the study of similar molecules to validate the proposed model and the accompanying mathematical formalism. Additional experimental data on other molecules would provide an opportunity to test the developed analytical approach, and it would further expand the knowledge of the pseudorotation in non-aromatic five-membered rings.

Unfortunately, many molecules belonging to the family of five-membered rings are not suitable for experimental studies in the submillimeter wave region. As mentioned above, the nearly freely pseudorotating molecule of cyclopentane [15,16] does not have a sufficient transition moment to be studied with the present apparatus. On the other hand, a number of heterocyclic molecules, previously studied in microwave, FIR, and Raman experiments, such as tetrahydrotiophene [17], silacyclopentane [18–21], tetrahydroselenophene [22], germacyclopentane [23], pyrrolidine [24–26], 2-cyclopenten-1-one [27], cyclopentanone [28], thiacyclopentane [29], 1,3-oxathiolane [30], and selenacyclopentane [31] have fairly large barriers to pseudorotation, and the molecules adopt rather rigid configurations. In such cases, the radial-angular coupling is fairly large, and pseudorotation is no longer a valid model of the vibrational motion [7].

1,3-Dioxolane (DOX), along with THF, appears to be a convenient object of study. Early IR studies [11] have shown that the DOX molecule (see Fig. 1) has properties similar to those of THF. Reduction of the molecular symmetry from D_{5h} symmetry in cyclopentane to C_{2v} (assuming planarity) in THF and DOX makes more PR transitions allowed, and heterocyclic sub stitutions in the molecular skeleton should result in appreciable transition moments.

Both molecules have a low barrier to pseudorotation [32], and comparable values of the pseudorotational constant $B_p = 3.19\,\mathrm{cm}^{-1}$, for THF, and $B_p = 3.99\,\mathrm{cm}^{-1}$ for DOX [11], but compared to THF, DOX has been given much less experimental attention. Baron and Harris [32] did study the rotational spectra of DOX in the microwave region and reported the observation of the purely rotational transitions in the lowest four states, as well as three c-type transitions connecting the $n = 0$ and $n = 1$ pseudorotational states. From the observed selection rules in the pseudorotational transitions and the analysis of the relative intensities of the low-J rotational transitions in the $n = 0$ and $n = 1$ states, they determined that the twisted configuration C_2 has higher energy than the bent one C_s. From the analysis of the transition frequencies, the A, B, and C rotational constants for the states $n = 0$–8, and the separation between the two lowest pseudorotational states, ΔE_{01} were determined. For a more detailed analysis, additional information concerning the positions of as many PR levels as possible, is desirable. Such information can be obtained from the study of the molecule in the submillimeter wave region where several pseudorotational bands, or parts thereof, can be observed, and the energy level structure of the appropriate PR states can be determined.

In the present work we report the experimental observation and the assignment of a total of 226 transitions belonging to three pseudorotational bands. These spectroscopic data, along with the previously reported microwave data, has been used to obtain a new set of molecular constants.

As in the case of THF, we have also carried out quantum chemistry calculations to complement our empirical determination of the PR surface from the spectroscopic data. The results of both methods will be discussed.

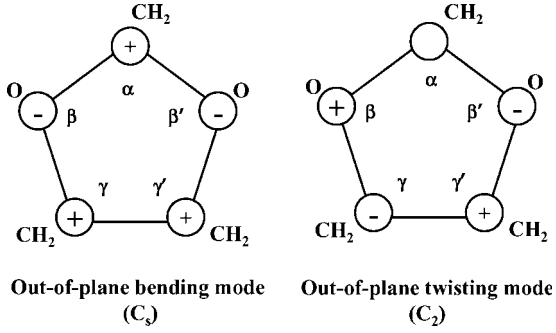

Fig. 1. The two out-of-plane bending modes in DOX whose interaction results in the pseudorotation. The Greek letters denote the carbon and oxygen atoms of the molecular skeleton used for the definition of the pseudorotational angle, see text for the details.

2. Experimental details

The spectra were obtained using the pulsed FASSST spectrometer described elsewhere [33]. To prepare the sample, compressed neon was run over the surface of liquid DOX. The temperature of the liquid DOX sample was varied in the range of 265–298 K, and the optimal conditions were found at 278 K. The sample prepared under these conditions was injected into the chamber through a pulsed valve. We have used different valve arrangements to adjust the experimental conditions to a particular task. To observe low-J transitions in $n = 0 \rightarrow 3$ band, a simple valve with a circular orifice (General Valve adapter 0.45 mm in diameter) has been

used. The background pressure was varied in the range of 35–100 psi, which resulted in rotational temperature of the sample as low as 3 K. To observe the high-J transitions, a slit nozzle with slit width 25 μm, and length 18 mm was used [14]. The latter arrangement produced a sample with temperatures of about 10–15 K. The microwave radiation was focused on the molecular jet and then collected by an InSb detector operating at liquid helium temperature. The signal output was averaged over 200–1000 scans, which corresponds to integration times of 100–500 μs per data point.

3. Experimental results and analysis

3.1. Spectroscopic observations

Although pseudorotation in five-membered rings is a two-dimensional problem, in the limit of free pseudorotation, the radial and angular parts of the pseudorotational Hamiltonian exactly separate, and are treated independently [34]. If a barrier to pseudorotation is introduced, it results in an interaction between the angular and radial modes. However, if the barrier is small, and the pseudorotation is lightly hindered, such interactions can be treated as perturbations. Since the radial motion is considerably higher in frequency than pseudorotation [11], and in this study we deal only with the lowest pseudorotational states that lie far below the excited radial states, reducing the problem to a one-dimensional provides a useful approximation [30]. The interaction with the radial mode can be treated, along with the interactions with other vibrational modes, using second-order perturbation theory [35].

It is therefore a common spectroscopic practice to represent the measured PR levels as the eigenvalues of a hindered PR Hamiltonian of the form

$$H_{\mathrm{PR}} = B_p \ell^2 + \frac{1}{2}\sum_j V_{2j}(1 - \cos 2j\phi), \tag{1}$$

where ℓ is the pseudorotational quantum number in the limit of free pseudorotation, i.e., when all terms, V_{2j}, of the potential are zero. Baron and Harris [32] were able to obtain the parameters B_p, V_2, and V_4 from the analysis of the perturbations in the frequencies of the rotational transitions, relative intensities thereof, and the frequency of the observed $n = 0 \rightarrow 1$ PR band. We have used predictions of the energies of the PR levels from the parameters obtained by Baron and Harris as a starting point for our spectroscopic studies of DOX. The c-type $n = 0 \rightarrow 1$ band, observed by these authors at about 68 GHz was expected to have transitions, with low J values of the R-branch, accessible by our spectrometer. The search in the lowest accessible part of the spectral range, between 153 and 220 GHz, resulted in the observation of several groups of transitions very similar to those corresponding to K-structure of the transitions with the same J'' in the P- or R-branch of the c-type band in THF (see Fig. 3 in our previous work [14]). The stick plot diagram of the observed spectrum is shown in Fig. 2.

Using the molecular constants reported by Baron and Harris [32], some of the observed groups of lines were

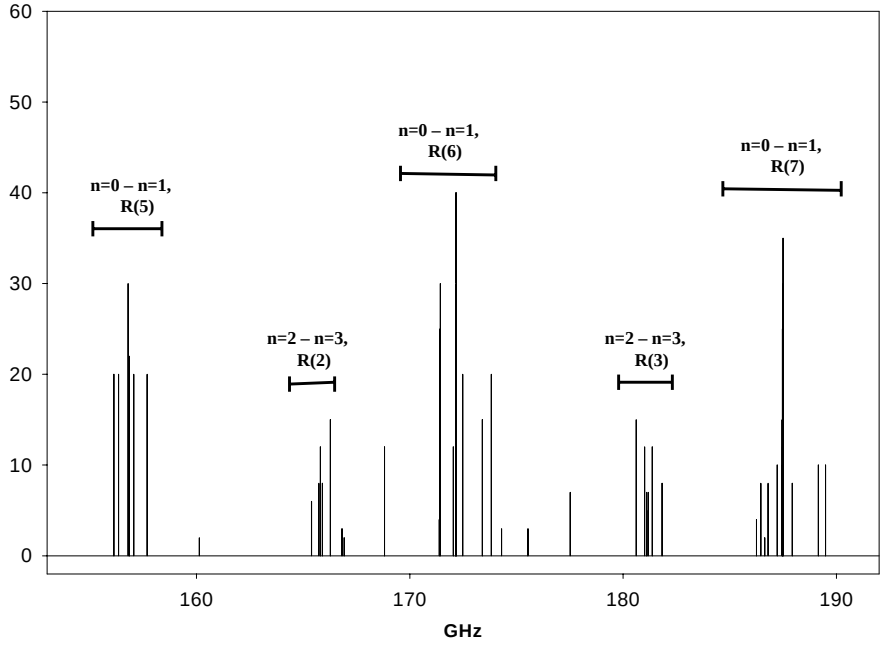

Fig. 2. The stick plot of the spectrum showing parts of the K-structure of the R-branch transitions belonging to the $n = 0 \rightarrow 1$ and $n = 2 \rightarrow 3$ c-type PR bands in DOX. The origins of these bands are located at 64840.46 and 119731.04 MHz, respectively, and are not accessible in the present experiment.

identified as belonging to the R-branch of the $n = 0 \rightarrow 1$ PR band with $J'' = 5$–9. From the predicted values of the energies and symmetry properties of the few lowest states [32], one would also expect a portion of another c-type band, corresponding to a transition between $n = 2$ and $n = 3$, to be observable in the same spectral region. By the comparison of the pattern of the calculated spectrum of the latter band with the observed structure of groups of transitions not assigned to $n = 0 \rightarrow 1$ band, we have identified most of the rest of the transitions in the 153–220 GHz region as belonging to the R-branch of the $n = 2 \rightarrow 3$ band with $J'' = 2$–5.

Additionally, a number of transitions were observed in the range between 260 and 364 GHz. These transitions are weaker than those belonging to the $n = 0 \rightarrow 1$ and $n = 2 \rightarrow 3$ bands. A set of transitions in the range between 290 and 330 GHz were consistently observed even using the expansion through a circular nozzle at high (up to 7 bar) backing pressures, resulting in expansion temperatures as low as 3 K. Therefore, it was concluded that these transitions likely originate from the lowest PR states. The observed transitions in this region do not follow the pattern typical for the c-type band. The results of the simulation of the spectra based on the reported [32] values of the rotational constants of DOX indicated that these transitions could belong to either an a-type or b-type band. Such selection rules are consistent with those derived by Greenhouse and Strauss [11] for $\Delta\ell = \pm 2$ PR transition. The stick plot diagram of the observed spectrum in the discussed region is shown in Fig. 3.

3.2. Hamiltonian

For the rotational analysis of the spectra we have used a rotational Hamiltonian similar to that used for THF [12,14,36]. However, it should be noted that in case of THF, the observed PR states were grouped in two pairs of relatively closely spaced levels, with the pairs separated by a relatively large energy gap. Therefore, the interactions between levels in different "doublets" were ignored. In DOX, the situation is different. According to a prediction using the constants of Baron and Harris [32], in DOX the lowest four eigenvalues of H_{PR} which are labelled by n, are spaced fairly evenly, with separations between adjacent states varying between 2 and 4 cm^{-1}. In such a case it is not possible to select any pairs of hindered n states and limit the analysis of the interactions to within such pairs. On the other hand, the next excited state, $n = 4$, is predicted about 20 cm^{-1} above $n = 3$. Therefore, in the rotational analysis of the observed spectra we have included the interactions between all the hindered PR levels within the manifold $n = 0$–3, and ignored all interactions with higher lying vibrational and hindered PR states.

At this level of approximation, the rotational Hamiltonian is written as follows:

$$n = \begin{matrix} 0 & 1 & 2 & 3 \end{matrix}$$

$$H_{Rot} = \begin{pmatrix} H_{00}+E_0 & H_{01} & H_{02} & H_{03} \\ H_{01} & H_{11}+E_1 & H_{12} & H_{13} \\ H_{02} & H_{12} & H_{22}+E_2 & H_{23} \\ H_{03} & H_{13} & H_{23} & H_{33}+E_3 \end{pmatrix}, \qquad (2)$$

where E_n are the eigenvalues of H_{PR} and [36]

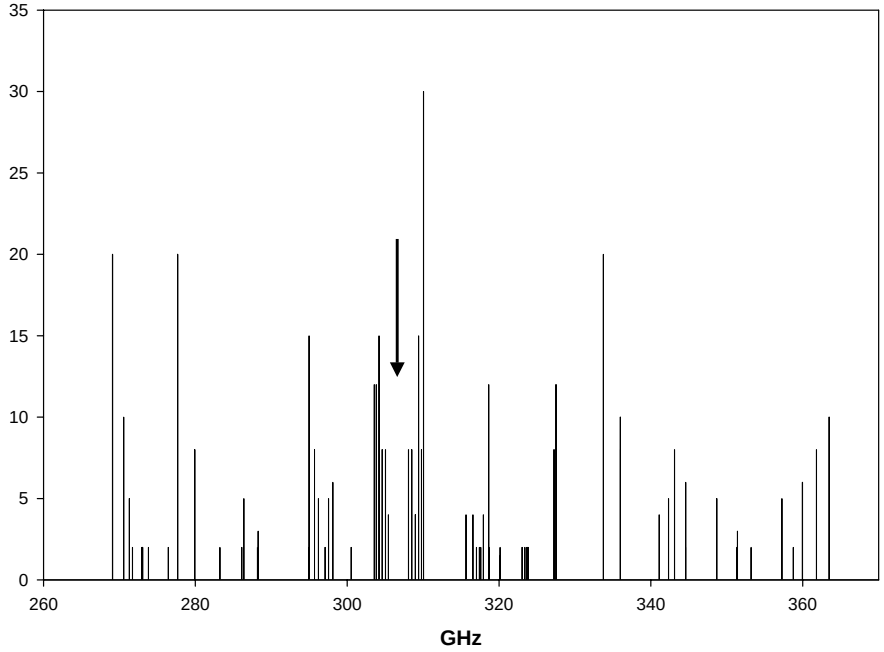

Fig. 3. The stick plot of the spectrum of the $n = 0 \rightarrow 3$ a-type PR band in DOX. The origin of the band is located at 306804.36 MHz and its position is indicated by an arrow.

$$
\begin{aligned}
H_{ii} &= A(i)P_a^2 + B(i)P_b^2 + C(i)P_c^2 - \Delta_J(i)(P^2)^2 \\
&\quad - \Delta_{JK}(i)P_a^2P^2 - \Delta_K(i)\left(P_a^2\right)^2 - 2\delta_J(i)P^2P_-^2 \\
&\quad - \delta_K(i)\left(P_a^2P_-^2 + P_-^2P_a^2\right) + H_J(i)P^6 \\
&\quad + H_{JK}(i)P^4P_a^2 + H_{KJ}(i)P^2P_a^4 + H_K(i)P_a^6 \\
&\quad + 2h_J(i)P^4P_-^2 + h_{JK}(i)P^2\left(P_a^2P_-^2 + P_-^2P_a^2\right) \\
&\quad + h_K(i)\left(P_a^4P_-^2 + P_-^2P_a^4\right), \\
P_-^2 &= P_b^2 - P_c^2,
\end{aligned} \tag{3}
$$

with

$$
H_{ij} = \left[F_{xy}(i,j) + F'_{xy}(i,j)P^2\right](P_xP_y + P_yP_x), \quad i \neq j, \tag{4}
$$

where x, y are dummy indexes for the inertial axes. The appropriate axes in Eq. (4) are chosen such that the term H_{ij} is allowed by symmetry

$$
\Gamma(\Psi(i)) \otimes \Gamma(H_{ij}) \otimes \Gamma(\Psi(j)) \supset A_1, \tag{5}
$$

where $\Psi(i)$ and $\Psi(j)$ represent the eigenfunctions of H_{PR}. At this point we made an assumption (which we will justify later) that the PR states labelled as $n = 0, 1, 2, 3$ in Eq. (2) are indeed the four lowest states and no other PR states are present in the vicinity of the manifold in question. Using this assumption as well as the symmetry properties of the four lowest PR states derived from the solution of the pseudorotational Schrödinger equation with the Hamiltonian, Eq. (1), and the values of B_p, V_2, and V_4 reported by Baron and Harris [32]

$$
\begin{aligned}
&\Gamma(\Psi(n=0)) = A_1, \\
&\Gamma(\Psi(n=1)) = B_1, \\
&\Gamma(\Psi(n=2)) = A_2, \\
&\Gamma(\Psi(n=3)) = B_2,
\end{aligned} \tag{6}
$$

we have determined the appropriate symmetry adopted expression for the non-vanishing coupling terms H_{ij} in Eq. (4)

$$
H_{ij} = \begin{cases}
\left[F_{bc}(i,j) + F'_{bc}(i,j)P^2\right](P_bP_c + P_cP_b), & (i,j) = 0,1, \\
\left[F_{ab}(i,j) + F'_{ab}(i,j)P^2\right](P_aP_b + P_bP_a), & (i,j) = 1,2, \\
\left[F_{bc}(i,j) + F'_{bc}(i,j)P^2\right](P_bP_c + P_cP_b), & (i,j) = 2,3, \\
\left[F_{ac}(i,j) + F'_{ac}(i,j)P^2\right](P_aP_c + P_cP_a), & (i,j) = 0,2, \\
\left[F_{ac}(i,j) + F'_{ac}(i,j)P^2\right](P_aP_c + P_cP_a), & (i,j) = 1,3, \\
\left[F_{ab}(i,j) + F'_{ab}(i,j)P^2\right](P_aP_b + P_bP_a), & (i,j) = 0,3.
\end{cases} \tag{7}
$$

3.3. Rotational assignment and analysis

For DOX, only the molecular constants A, B, and C are available from the previous studies [32], therefore it was possible to make definitive assignments for only a fraction of the observed lines by simple comparison of the observed spectrum with one simulated using the rotational Hamiltonian H_{rot} with the all constants except A, B, and C fixed at zero. Since only portions of the R-branches were observed, it was not possible to use combination differences to make the assignment of other transitions.

To complete the analysis, the following approach was used. A spectrum of the $n = 0 \rightarrow 1$ band was generated using the CALFIT package [37] and the set of rotational constants for the states $n = 0$–3, reported by Baron and Harris [32]. Comparing the simulated pattern with the experimental data, a portion of the newly observed lines were assigned. These newly assigned submillimeter wave transitions, along with the raw data obtained by Baron and Harris, were used in the subsequent fit, where terms in Eqs. (3) and (7), relevant to the PR states $n = 0, 1$ were introduced and optimized. The resulting set of molecular constants was used to produce the next generation of simulated spectrum, which was subsequently compared to the experimental data. As a result, more of the lines were assigned and added to the input data set. A similar iterative approach was used to analyze the transitions in the $n = 2 \rightarrow 3$ band. At this point, the two bands were analyzed separately, and the coupling terms, H_{ij}, connecting rotational levels in PR states $n = 0, 1$ with levels in PR states $n = 2, 3$ were not included. Such an iterative approach allowed us to assign the majority of the observed transitions and generate preliminary sets of molecular constants in the states $n = 0$–3.

To analyze the spectral pattern observed around 306 GHz (Fig. 3), we noted that according to the selection rules of Greenhouse and Strauss [11] and predictions of Baron and Harris [32], an a-type $n = 0 \rightarrow 3$ band, correlating with a $\Delta\ell = \pm 2$ transition is expected to be observed at about $8.47\,\mathrm{cm}^{-1}$. Using the sets of constants obtained from the analysis of the $n = 0 \rightarrow 1$ and $n = 2 \rightarrow 3$ bands as described above, we generated a spectral pattern for such a band, and found that the observed spectrum was similar to the predicted pattern. Using the correlation between the predicted and observed spectrum, as well as a combination differences analysis for the low-J transitions, we were able to make the assignments of a portion of the observed lines in this band. These newly assigned transitions were added to the data set and used in a global fit along with the previously assigned submillimeter wave transitions in $n = 0 \rightarrow 1$ and $n = 2 \rightarrow 3$ bands, and those reported by Baron and Harris, and the coupling terms between states in the pairs $n = 0, 1$ and $n = 2, 3$ (H_{02}, H_{13}, etc.) were introduced. An iterative process, similar to that which has been described above, was used in the global fit to assign more observed transitions and refine the molecular constants. The frequencies of the assigned transitions in the bands $n = 0 \rightarrow 1$, $n = 2 \rightarrow 3$, $n = 0 \rightarrow 3$ are given in Tables 1–3, respectively. A total of 48 microwave transitions available from Baron and Harris work, and 226 submillimeterwave transitions observed and assigned in this work, were fit to the

Table 1
Experimentally observed rotational transitions in R-branch of the $n = 0 \rightarrow 1$ pseudorotational band in DOX

$J'(K_a', K_c')$–$J''(K_a'', K_c'')$	f (MHz)	$f_e - f_c$ (MHz)
6(5,1)–5(4,1)	156128.8	0.66
6(4,2)–5(3,2)	156346.1	−0.29
6(3,3)–5(2,3)	156792.0	−0.82
6(4,3)–5(3,3)	156845.0	0.33
6(2,4)–5(1,4)	156851.1	−0.02
6(5,2)–5(4,2)	157058.6	0.12
6(6,0)–5(5,0)	157689.1	0.76
7(5,2)–6(4,2)	171410.6	−0.19
7(6,1)–6(5,1)	171429.2	0.32
7(4,3)–6(3,3)	172035.0	−0.40
7(5,3)–6(4,3)	172152.1	−0.24
7(1,6)–6(0,6)	172158.5	0.21
7(2,6)–6(1,6)	172158.5	0.21
7(3,4)–6(2,4)	172160.6	0.25
7(4,4)–6(3,4)	172164.2	0.05
7(2,5)–6(1,5)	172175.0	0.07
7(3,5)–6(2,5)	172175.0	0.05
7(6,2)–6(5,2)	172479.7	0.06
7(7,0)–6(6,0)	173396.8	0.10
7(7,1)–6(6,1)	173818.2	−0.10
8(6,2)–7(5,2)	186455.1	−0.19
8(7,1)–7(6,1)	186791.7	0.31
8(5,3)–7(4,3)	187222.7	−0.14
8(4,4)–7(3,4)	187449.5	−0.26
8(6,3)–7(5,3)	187454.3	−0.24
8(5,4)–7(4,4)	187459.8	−0.54
8(1,7)–7(0,7)	187466.3	−0.43
8(2,7)–7(1,7)	187466.3	−0.43
8(3,5)–7(2,5)	187491.6	0.24
8(4,5)–7(3,5)	187491.6	0.16
8(2,6)–7(1,6)	187494.0	0.63
8(3,6)–7(2,6)	187494.1	0.63
8(7,2)–7(6,2)	187924.6	−0.75
8(8,0)–7(7,0)	189151.1	−0.09
8(8,1)–7(7,1)	189488.7	−0.41
9(7,2)–8(6,2)	201507.0	0.00
9(8,1)–8(7,1)	202232.2	−0.01
9(6,3)–8(5,3)	202342.2	0.60
9(5,4)–8(4,4)	202713.0	−0.13
9(6,4)–8(5,4)	202739.0	0.07
9(7,3)–8(6,3)	202755.6	0.12
9(1,8)–8(0,8)	202778.0	0.56
9(2,8)–8(1,8)	202778.0	0.56
9(4,5)–8(3,5)	202792.3	0.30
9(2,7)–8(1,7)	202812.2	−0.89
9(3,7)–8(2,7)	202812.3	−0.89
9(3,6)–8(2,6)	202816.0	−0.06
9(4,6)–8(3,6)	202816.0	−0.07
9(8,2)–8(7,2)	203398.4	−0.12
9(9,0)–8(8,0)	204932.4	0.56
9(9,1)–8(8,1)	205187.0	0.32
10(8,2)–9(7,2)	216587.8	−0.15
10(9,1)–9(8,1)	217762.8	−0.12
10(6,4)–9(5,4)	217942.6	−0.24
10(7,4)–9(6,4)	217998.1	−0.16
10(8,3)–9(7,3)	218060.7	0.52
10(6,5)–9(5,5)	218072.3	−0.27
10(5,5)–9(4,5)	218073.0	0.38
10(10,0)–9(9,0)	220725.0	−0.03
10(10,1)–9(9,1)	220908.0	−0.27

The difference between the experimentally observed (f_e) and calculated (f_c) frequencies are given. The experimental uncertainty is 0.5 MHz.

Table 2
Experimentally observed rotational transitions in R-branch of the $n = 2 \rightarrow 3$ pseudorotational band in DOX

$J'(K_a', K_c')$–$J''(K_a'', K_c'')$	f (MHz)	$f_e - f_c$ (MHz)
3(2,1)–2(1,1)	165389.5	0.20
3(1,2)–2(0,2)	165738.0	0.46
3(2,2)–2(1,2)	165808.7	1.10
3(3,1)–2(2,1)	166275.0	−0.13
4(3,1)–3(2,1)	180612.5	−0.39
4(2,2)–3(1,2)	181005.5	−0.45
4(1,3)–3(0,3)	181108.9	−0.24
4(2,3)–3(1,3)	181113.1	−0.16
4(3,2)–3(2,2)	181183.1	−0.27
4(4,0)–3(3,0)	181365.8	0.01
4(4,1)–3(3,1)	181825.8	−0.21
5(4,1)–4(3,1)	195850.0	−0.02
5(3,2)–4(2,2)	196217.1	0.04
5(2,3)–4(1,3)	196436.0	−0.09
5(1,4)–4(0,4)	196436.0	0.27
5(2,4)–4(1,4)	196436.0	0.09
5(3,3)–4(2,3)	196450.7	−0.01
5(4,2)–4(3,2)	196570.9	0.10
5(5,0)–4(4,0)	196904.1	0.78
5(5,1)–4(4,1)	197401.1	0.13
6(5,1)–5(4,1)	211110.3	−0.42
6(4,2)–5(3,2)	211369.6	0.11
6(3,3)–5(2,3)	211740.0	−0.27
6(1,5)–5(0,5)	211749.4	0.43
6(2,5)–5(1,5)	211749.4	0.42
6(2,4)–5(1,4)	211769.9	−0.22
6(3,4)–5(2,4)	211770.8	−0.09
6(4,3)–5(3,3)	211779.6	−0.32
6(5,2)–5(4,2)	211973.1	−0.23
6(6,0)–5(5,0)	212514.5	0.22
6(6,1)–5(5,1)	213002.9	0.37
7(6,1)–6(5,1)	226407.2	−0.28
7(5,2)–6(4,2)	226474.4	0.62
7(4,3)–6(3,3)	227012.1	−0.05
7(2,5)–6(1,5)	227084.1	0.67
7(2,5)–6(1,5)	227084.1	0.67
7(3,4)–6(2,4)	227092.8	0.12
7(4,4)–6(3,4)	227095.6	0.09
7(5,3)–6(4,3)	227102.1	−0.00
7(6,2)–6(5,2)	227394.5	−0.45
7(7,0)–6(6,0)	228192.8	0.05
7(7,1)–6(6,1)	228633.1	0.75
8(8,0)–7(7,0)	243923.1	−0.42
8(8,1)–7(7,1)	244291.1	0.39
9(7,2)–8(6,2)	256625.1	−0.04
9(1,8)–8(0,8)	257626.1	−0.22
9(2,8)–8(1,8)	257626.1	−0.22
11(1,10)–10(0,10)	288175.6	0.04
11(2,10)–10(1,10)	288175.6	0.04

The difference between the experimentally observed (f_e) and calculated (f_c) frequencies are given. The experimental uncertainty is 0.5 MHz.

Hamiltonian equation (2). The standard deviation of the fit was 307 kHz. Unlike the case of THF, the microwave and submillimeterwave transitions were equally weighted since the instrumental accuracy of the Baron and Harris measurements is not reported. The molecular parameters resulting from the fit are summarized in Table 4.

Table 3
Experimentally observed rotational transitions in the $n = 0 \rightarrow 3$ pseudorotational band in DOX

$J'(K'_a, K'_c)$–$J''(K''_a, K''_c)$	f (MHz)	$f_e - f_c$ (MHz)
P-branch		
5(1,4)–6(1,5)	245196.8	−0.05
4(2,2)–5(2,3)	246860.5	−0.13
4(3,2)–5(3,3)	247092.0	−0.20
2(1,2)–3(3,1)	249682.4	−0.27
3(3,0)–4(3,1)	250264.5	0.45
5(0,5)–6(0,6)	251946.3	−0.17
5(1,5)–6(1,6)	251946.3	−0.17
4(1,3)–5(1,4)	253755.8	0.41
4(2,3)–5(2,4)	253760.2	0.41
3(3,1)–4(3,2)	256371.9	0.35
2(1,1)–3(3,0)	256834.3	0.34
4(0,4)–5(0,5)	260515.6	−0.02
4(1,4)–5(1,5)	260515.6	−0.04
3(1,2)–4(1,3)	262282.2	−0.33
3(2,2)–4(2,3)	262362.2	−0.27
2(2,0)–3(2,1)	264999.5	−0.72
3(0,3)–4(0,4)	269088.7	0.36
3(1,3)–4(1,4)	269089.4	0.40
2(1,1)–3(1,2)	270568.8	0.73
2(2,1)–3(2,2)	271307.8	0.29
1(0,1)–2(2,0)	272540.8	0.38
2(0,2)–3(0,3)	277657.3	−0.02
2(1,2)–3(1,3)	277673.7	0.04
1(1,0)–2(1,1)	279909.8	−0.18
1(0,1)–2(0,2)	286123.7	0.01
1(0,1)–2(0,2)	286123.7	0.01
1(1,1)–2(1,2)	286382.5	−0.07
0(0,0)–1(0,1)	294974.6	−0.57
Q-branch		
9(0,9)–9(2,8)	249556.6	0.10
9(1,9)–9(1,8)	249556.7	0.10
7(0,7)–7(2,6)	262959.6	−0.39
7(1,7)–7(1,6)	262959.6	−0.39
8(1,7)–8(3,6)	263046.0	−0.62
8(2,7)–8(2,6)	263046.0	−0.62
6(1,6)–6(1,5)	269689.6	0.55
7(1,6)–7(3,5)	269758.3	0.90
7(2,6)–7(2,5)	269758.3	0.85
8(2,6)–8(4,5)	269845.2	0.42
8(3,6)–8(3,5)	269845.3	0.21
5(1,5)–5(1,4)	276427.3	−0.25
6(1,5)–6(3,4)	276483.9	−0.10
6(2,5)–6(2,4)	276485.1	−0.04
7(2,5)–7(4,4)	276559.8	−0.02
7(3,5)–7(3,4)	276563.9	−0.06
4(0,4)–4(2,3)	283171.4	−0.03
4(1,4)–4(1,3)	283176.7	−0.07
5(1,4)–5(3,3)	283216.0	−0.09
5(2,4)–5(2,3)	283237.4	−0.05
6(2,4)–6(4,3)	283273.6	0.05
6(3,4)–6(3,3)	283337.6	0.13
7(3,4)–7(5,3)	283339.7	0.01
8(4,4)–8(6,3)	283404.9	−0.24
7(4,4)–7(4,3)	283498.2	−0.11
5(2,3)–5(4,2)	289766.3	−0.10
4(1,3)–4(3,2)	289850.5	0.02
3(1,3)–3(1,2)	289977.8	−0.08
4(2,3)–4(2,2)	290133.3	0.01
5(3,3)–5(3,2)	290418.7	−0.10
6(4,3)–6(4,2)	290875.0	−0.29
8(6,3)–8(6,2)	292385.2	0.03
6(4,2)–6(6,1)	292424.0	−0.22
5(3,2)–5(5,1)	293865.8	−0.38
4(2,2)–4(4,1)	294935.8	−0.50
3(1,2)–3(3,1)	295693.7	−0.21
2(0,2)–2(2,1)	296200.0	0.04
2(1,2)–2(1,1)	297094.4	−0.17
3(2,2)–3(2,1)	297533.2	−0.26
4(3,2)–4(3,1)	298108.4	−0.45
5(4,2)–5(4,1)	298809.4	−0.42
6(5,2)–6(5,1)	299619.6	−0.23
7(6,2)–7(6,1)	300515.0	0.00
8(7,2)–8(7,1)	301463.6	0.12
1(1,1)–1(1,0)	303560.5	0.20
2(2,1)–2(2,0)	303827.1	0.27
3(3,1)–3(3,0)	304190.0	−0.35
4(4,1)–4(4,0)	304609.5	−0.09
5(5,1)–5(5,0)	305036.5	0.02
6(6,1)–6(6,0)	305426.1	−0.36
6(6,0)–6(6,1)	308066.3	0.27
5(5,0)–5(5,1)	308511.2	0.48
4(4,0)–4(4,1)	308972.5	0.06
3(3,0)–3(3,1)	309410.3	0.50
2(2,0)–2(2,1)	309780.1	−0.21
1(1,0)–1(1,1)	310047.8	−0.21
4(3,1)–4(3,2)	315648.8	0.29
2(1,1)–2(1,2)	316557.8	0.00
2(2,1)–2(0,2)	317410.1	0.06
3(3,1)–3(1,2)	317924.3	−0.13
4(4,1)–4(2,2)	318698.7	−0.06
6(4,2)–6(4,3)	323035.0	0.17
5(3,2)–5(3,3)	323381.5	0.35
4(2,2)–4(2,3)	323585.3	0.01
3(1,2)–3(1,3)	323685.0	0.11
3(2,2)–3(0,3)	323771.1	0.14
4(3,2)–4(1,3)	323843.3	0.03
R-branch		
1(0,1)–0(0,0)	318644.2	0.14
2(1,2)–1(1,1)	327232.6	0.03
2(0,2)–1(0,1)	327507.8	−0.11
2(1,1)–1(1,0)	333735.3	−0.14
3(1,3)–2(1,2)	335967.6	−0.03
3(0,3)–2(0,2)	335985.9	0.04
2(2,0)–1(0,1)	341088.1	−0.20
3(2,2)–2(2,1)	342313.8	0.23
3(1,2)–2(1,1)	343105.8	0.04
4(1,4)–3(1,3)	344578.6	−0.50
4(0,4)–3(0,3)	344580.0	0.13
3(2,1)–2(2,0)	348684.8	0.59
4(2,3)–3(2,2)	351314.0	−0.02
4(1,3)–3(1,2)	351403.3	−0.04
5(0,5)–4(0,4)	353186.5	−0.15
5(1,5)–4(1,4)	353186.5	−0.13
4(3,2)–3(3,1)	357254.4	−0.23
4(2,2)–3(2,1)	358756.3	0.05
5(2,4)–4(2,3)	359962.2	0.13
5(1,4)–4(1,3)	359967.3	0.10
6(1,6)–5(1,5)	361798.5	0.14
6(0,6)–5(0,5)	361798.5	0.14
4(3,1)–3(3,0)	363467.0	−0.34
4(3,1)–3(3,0)	363467.0	−0.34

The difference between the experimentally observed (f_e) and calculated (f_c) frequencies are given. The experimental uncertainty is 0.5 MHz.

Table 4
Molecular constants of 1,3-dioxolane

Constant	0	1	2	3
A (MHz)	7827.170(34)	7834.8288(252)	7812.74214(209)	7821.24843(148)
B (MHz)	7534.4595(241)	7525.3222(155)	7553.53408(184)	7544.09177(128)
C (MHz)	4294.4890(153)	4290.5931(185)	4301.2353(34)	4296.1140(34)
Δ_J (kHz)	3.684(224)	4.112(175)	1.8191(185)	2.1644(104)
Δ_{JK} (kHz)	12.13(164)	10.96(154)	52.892(86)	7.531(65)
Δ_K (kHz)	−12.77(196)	−9.99(197)	51.458(312)	9.459(309)
δ_J (kHz)	0.929(271)	0.769(134)	−2.195(134)	−2.436(62)
δ_K (kHz)	−56.8(147)	−153.9(107)	196.4(42)	171.33(194)
H_J (Hz)	–	–	−4.41(44)	3.454(186)
H_{JK} (Hz)	−45.9(214)	−267(56)	−15.73(206)	−18.59(116)
H_{KJ} (Hz)	–	660(182)	−121.9(94)	−100.0(69)
H_K (Hz)	107.4(283)	−273(133)	170.3(130)	166.0(101)
h_J (Hz)	–	–	−99.96(280)	−64.46(103)
h_{JK} (Hz)	502(261)	637(130)	210(137)	1078(43)
h_K (kHz)	–	−2.28(81)	1.743(98)	0.264(33)
$H_{ij}(i,j)$ coupling terms				
$F_{bc}(0,1)$ (MHz)	−13.93(58)		$F_{ac}(0,2)$ (MHz)	−33.297(161)
$F'_{bc}(0,1)$	–		$F'_{ac}(0,2)$ (kHz)	8.4(38)
$F_{ab}(1,2)$ (MHz)	−20.448(208)		$F_{ac}(1,3)$ (MHz)	−6.56 (55)
$F'_{ab}(1,2)$ (kHz)	138.0(47)		$F'_{ac}(1,3)$ (kHz)	271.1(93)
$F_{bc}(2,3)$ (MHz)	36.946(39)		$F_{ab}(0,3)$ (MHz)	13.99(258)
$F'_{bc}(2,3)$ (kHz)	−49.96(79)		$F'_{ab}(0,3)$ (kHz)	−225(41)
PR level energies				
E_1 (MHz)	64840.437(98)			
E_2 (MHz)	187071.3348(310)			
E_3 (MHz)	306804.2108(301)			

3.4. Potential surface and rotational constant analysis

The preceding assignment and the resulting fit of the observed transitions allows a more definite conclusion to be drawn about the symmetries of the observed PR levels, tentatively labelled $n = 0$–3, than was possible previously. The DOX molecule is a near-oblate asymmetric top exhibiting large amplitude out-of-plane vibrations, and is appropriately described by a PI symmetry group isomorphous with the C_{2v} point group. The components of its dipole moment transform as $\Gamma(\mu_a) = B_2$, $\Gamma(\mu_b) = A_1$, and $\Gamma(\mu_c) = B_1$ (note that compared to THF, the a and b axes are "switched," and the b axis coincides with the C_2 axis of the DOX molecule). The observed c-type transitions between $n = 0$ and $n = 1$, as well as between $n = 2$ and $n = 3$, require that $\Gamma(\Psi(n=0)) \otimes \Gamma(\Psi(n=1)) \supset B_1$ and $\Gamma(\Psi(n=2)) \otimes \Gamma(\Psi(n=3)) \supset B_1$. Since the ground $n = 0$ PR state is totally symmetric (A_1), it immediately follows that the $\Gamma(\Psi(n=1)) = B_1$, and correlates with the $|\ell| = 1$ free pseudorotor level [11]. On the other hand, the a-type transition between $n = 0$ and $n = 3$ requires that $\Gamma(\Psi(n=3)) = B_2$ and correlates with the $|\ell| = 2$ free pseudorotor level. Hence, to be connected with the $n = 3$ level by a c-type transition, the state $n = 2$, lying below the one labelled $n = 3$, should transform as A_2, and correlate with the $|\ell| = 1$. The observed selection rules are illustrated in Fig. 4, and are consistent with the symmetries of the observed states, given by Eq. (6). These presently derived symmetries are identical, for the four lowest states, as those derived from the model potential of Baron and Harris. This is unlike our work [14] on THF where our symmetry assignments were distinctly different from those previously reported [12].

Similarly to THF, in DOX both states correlating with $|\ell| = 1$ have been observed, but only one with $|\ell| = 2$. To derive the shape of the barrier to pseudorotation, it is necessary to establish the symmetry ordering of the four lowest PR states. Therefore, it is necessary to verify that the four observed PR levels are the four lowest levels, and we have not observed a transition to a PR level with the $n > 3$. The above argument based on selection rules establishes that the PR states $n = 0, 1, 2$, correlating with non-degenerate $|\ell| = 0$ and doubly degenerate $|\ell| = 1$, respectively, are indeed the three lowest states. To estimate the energy of the other state ($n = 4$), correlating with the $|\ell| = 2$, we follow an argument similar to that which has been invoked in case of THF [14]. The sum of the energy gaps ΔE_{23} and ΔE_{24} can be estimated as $6B_p - |V_2|/2 = 18.84\,\mathrm{cm}^{-1}$. Given the experimental value of $\Delta E_{23} = 3.99\,\mathrm{cm}^{-1}$, we conclude that the $n = 4$ state lies approximately $15\,\mathrm{cm}^{-1}$ above the $n = 2$ state, and therefore, has higher energy than the assigned $n = 3$ ($E_3 = 10.23\,\mathrm{cm}^{-1}$), therefore the four observed PR states are indeed the four lowest, and their symmetry ordering is given by Eq. (6), Table 5.

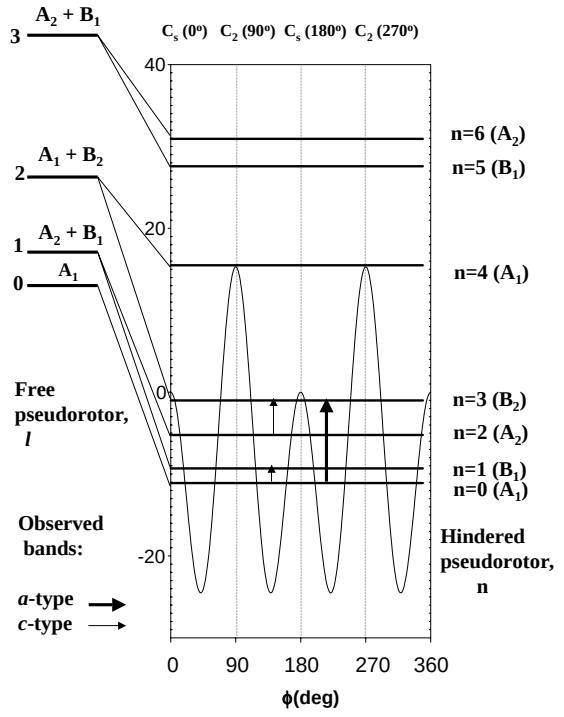

Fig. 4. The pseudorotational energy level diagram of DOX and its correlation to the free pseudorotor level (ℓ) structure. The empirical potential function for pseudorotation is derived from the experimental data, and constructed using the values of V_2 and V_4 in Table 8. The energy levels are drawn approximately to scale. The observed selection rules are shown by arrows as indicated.

Table 5
The instantaneous values of the rotational constants (in MHz) of DOX, derived by different methods

G^i	Model		
	G^0, G^2, G^4	B3LYP/ 6-31 + G**	MP2/ 6-31 + G**
A^0	7819.97(24)	7801.34(22)	7768.45(24)
A^2	39.73(105)	53.18(30)	44.57(36)
A^4	2.90(65)	−12.88(27)	−11.04(32)
A^6	–	−0.7(2)	6.66(30)
B^0	7541.35(36)	7510.37(21)	7510.29(24)
B^2	−47.54(157)	−65.17(31)	−57.74(36)
B^4	−11.99(98)	9.11(28)	8.36(32)
B^6	–	−3.88(31)	1.13(34)
C^0	4293.53(80)	4286.96(22)	4254.25(24)
C^2	−12.82(340)	−12.98(32)	−11.05(36)
C^4	−10.49(213)	−0.7(27)	−0.66(32)
C^6	–	2.42(31)	1.18(32)

The second column is the result of the fit of the experimentally obtained data to Eq. (10), truncated at G^4 term (see text for details). The last two columns are the Fourier expansions of the calculated functions $G(\phi)$, obtained at the different levels of theory.

We have shown previously [14,35], that if the magnitude of the terms V_2 and V_4 satisfy the condition [35]

$$32B_pV_4 + 2V_4^2 > V_2^2, \tag{8}$$

Table 6
The correlation between the signs of the leading terms in expansion equation (1) and the symmetry ordering of the lowest five PR states

PR state	$V_2 > 0$	$V_2 > 0$	$V_2 < 0$	$V_2 < 0$
n	$V_4 > 0$	$V_4 < 0$	$V_4 > 0$	$V_4 < 0$
0	A_1	A_1	A_1	A_1
1	B_1	B_1	A_2	A_2
2	A_2	A_2	B_1	B_1
3	A_1	B_2	A_1	B_2
4	B_2	A_1	B_2	A_1

i.e., $V_2 < 91$ cm^{-1} given the values of $B_p = 3.99\,\text{cm}^{-1}$, and $V_4 = 40\,\text{cm}^{-1}$ [32], the signs of these terms can be uniquely related to the symmetry ordering of the lowest PR states. This correlation is summarized in Table 6. Using these results and the symmetry properties of the lowest hindered PR states (Eq. (6)), we find that in case of DOX, $V_2 > 0$ and $V_4 < 0$.

The signs of the leading terms in the expansion of the potential barrier Eq. (1) and the symmetry ordering of the lowest states are consistent with the results obtained by Baron and Harris. The corresponding shape of the potential barrier is shown in Fig. 4. The profile of the PES exhibits two pairs of unequal maxima at symmetric configurations C_2 and C_s, the latter being higher in energy, and four equal minima in non-symmetric configurations.

The quantitative details of the empirical PES depend upon the measured hindered PR vibrational origins, which in turn determine numerical values for the V_2 and V_4 in H_{PR}. The energies of the lowest PR states and, therefore, the origin frequencies of the transitions within these states, are most sensitive to the details of the PES for pseudorotation. As it is shown in Table 7, the frequencies of bands $n = 0 \rightarrow 1$ and $n = 2 \rightarrow 3$ are predicted by Baron and Harris with reasonable accuracy, whereas the predicted energy of the level $n = 3$ is significantly lower than that measured in the present study. To refine the parameters of the barrier to pseudorotation, we have fit the totality of the experimentally observed frequencies of PR bands, as it has been done in the case of THF [14]. We have used the data obtained in the FIR studies by Greenhouse and Strauss [11], along with the data obtained in the present work. The results of the fit are given in Table 7.

Inspection of the residuals of the fit shows certain similarities with the case of THF. For the submillimeter wave data, the difference between the experimentally observed and predicted values of PR band origins are of the order of 0.2–0.4 cm^{-1}, as in the case of THF. For the FIR data, the fit produces residuals of the order of the experimental accuracy, with the exception of the origin of $n = 7 \rightarrow 10$ band, where the difference is about 1.2 cm^{-1}. Such a singular discrepancy may result from a local perturbation, or a measurement or assignment error.

Table 7
The experimental and predicted values of the origins of observed pseudorotational transitions in 1,3-dioxolane

$n' - n''$	F_{exp} (cm^{-1})	Baron and Harris [32]	This work
		$F_{exp} - F_{calc}$ (cm^{-1})	$F_{exp} - F_{calc}$ (cm^{-1})
1–0[a]	2.16	0.001	0.369
3–0[a]	10.23	1.76	0.14
3–2[a]	3.99	−0.05	−0.23
7–6[b]	24.80	0.91	0.48
9–8[b]	34.40	0.57	0.01
10–7[b]	38.00	0.82	1.2
11–10[b]	42.80	−0.69	−0.78
12–9[b]	43.60	−0.24	−0.27
13–12[b]	52.00	0.32	0.26
15–14[b]	60.10	0.33	0.31
17–16[b]	67.80	0.02	0.01
20–18[b]	74.80	−0.97	−0.98

The vibrational frequencies that were used to generate residuals in columns 3 and 4, were calculated from pseudorotational Hamiltonian H_{PR}, and the parameters of Baron and Harris ($B_p = 3.99\,cm^{-1}$, $V_2 = 10.2\,cm^{-1}$, $V_4 = -40.0\,cm^{-1}$), and the parameters obtained in the present work ($B_p = 3.99\,cm^{-1}$, $V_2 = 15.3\,cm^{-1}$, $V_4 = -31.9\,cm^{-1}$), respectively.

[a] This work.

[b] Greenhouse and Strauss [11].

Compared to THF, DOX has a larger value of the pseudorotational constant B_p which results in a lower density of states and a smaller number of levels being populated and experimentally observed. Lack of data for higher lying states in the present experiment does not permit more detailed modeling.

4. Quantum chemistry calculations

Considering the rapid improvement in quantum chemistry calculations it is useful to compare computations of the PES of a molecule with empirically derived one. For this purpose we have applied both the direct (i.e., computation of the energy values on the PES), and indirect (i.e., rotational constant analysis) methods [14] for DOX.

The pseudorotational angle is defined in terms of the two dihedral angles, τ and τ'. The dihedral angle τ is defined as the angle between the plane containing the α, γ, and γ' carbons (Fig. 1) and the plane containing the α and γ carbons and β oxygen. Similarly, τ' is the angle between the plane containing the α, γ, and γ' carbons and the plane containing the α and γ' carbons and β' oxygen. To obtain the energies on the PES and instantaneous values of the rotational constants at different values of the pseudorotational angle ϕ, a number of calculations were run, where τ was fixed, each time at a different value, and τ' was optimized such that the molecule assumed its minimal energy configuration. The profiles of the PES along the pseudorotation path, obtained from the direct calculations of values of the energy as the function of the pseudorotational angle are shown in Fig. 6, along with the corresponding curves resulting from the empirical fit. The computational results were also fit to the potential function in the Hamiltonian H_{PR}, and the corresponding values of the V_{2j} terms are given in Table 8.

The calculations show that both the empirical and quantum chemistry methods give an energy profile along the pseudorotational path with 4 equivalent global minima ϕ_g at non-symmetric configurations and two non-equivalent maxima at symmetric configurations. Similarly to the case of THF, the amplitude of the barrier calculated using the MP2 method is much larger than that calculated using B3LYP, and the latter method produces results rather similar to those derived empirically. However, the empirically calculated barrier has a higher energy at the twisted C_2 ($\phi = 90°$) configuration, whereas both computational methods predict the bent C_s ($\phi = 0°$) configuration to have higher energy, although the difference is very slight in the B3LYP calculations. In terms of the expansion coefficients in Eq. (1) the relative energies of the maxima at non-equivalent symmetric configurations are determined by the sign of V_2 term, that is if $V_2 > 0$, then $E(C_2) > E(C_s)$, and vise versa. As Table 8 shows, the expansion of the PES into a series Eq. (1) yields a negative V_2 value for both computational methods.

To gauge the reliability of the computational methods, it is instructive to also compare the rotational constants obtained computationally and experimentally. For this purpose, the values for $G(\phi)$ produced by quantum chemistry calculations, and experimentally observed values for the rotational constants G_n in the PR state n, are fit respectively to the following equations [14]:

$$G(\phi) = G^0 + G^2\cos(2\phi) + G^4\cos(4\phi) + \cdots, \tag{9}$$

$$G_n = G^0 + G^2\langle\Psi_n|\cos(2\phi)|\Psi_n\rangle + G^4\langle\Psi_n|\cos(4\phi)|\Psi_n\rangle + \cdots, \tag{10}$$

where $G = A,\ B,\ C$, and Ψ_n is the eigenfunction of the pseudorotational state n. The experimentally obtained rotational constants for states $n = 0$–3 obtained in this work, and for state $n = 4$, as reported by Baron and Harris, were used to obtain G^0, G^2, and G^4 terms in Eqs. (9) and (10). The results of the calculations are given in Fig. 5, and the terms of the expansion, G^i, are given in Table 5. The comparison of the calculated values (curves 2 and 3) of the rotational constants as functions of the pseudorotational angle using different methods shows reasonable agreement with the results obtained from the analysis of the experimental data (bold curve, 1). Similarly to the case of THF, the dependencies obtained from the MP2 and B3LYP computational methods are

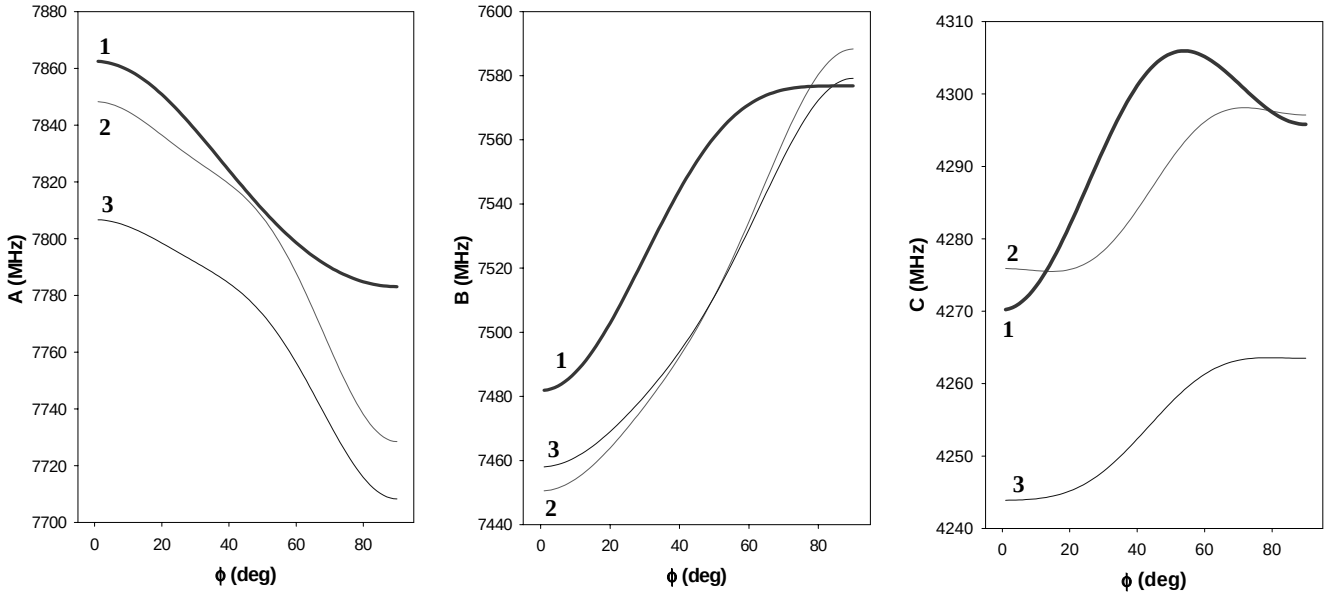

Fig. 5. The dependence of the instantaneous values of the rotational constants on the pseudorotational angle. 1 (bold curve): A fit of the experimentally observed values of the rotational constants in the lowest five states ($n = 0$–4) to the expansion equation (10) truncated at the G^4 term; curves 2 and 3: results of the ab initio calculations at the levels of B3LYP/6-31 + G** and MP2/6-31 + G**, respectively.

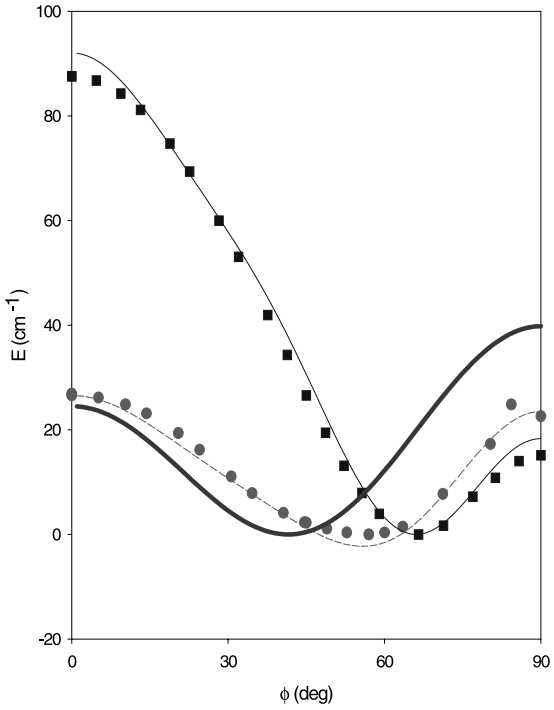

Fig. 6. A fragment of a PES function between the bent (C_s, $\phi = 0°$) and twisted (C_2, $\phi = 90°$) conformations of DOX. The bold curve corresponds to the empirically derived potential function (see full profile in Fig. 4); the circles and corresponding fit curve represents the potential function derived from density functional calculations B3LYP/6-31 + G**, the squares and the corresponding curve represent the results obtained from ab initio calculations at the MP2/6-31 + G** level. The values of the parameters V_{2j} required to represent each of the curves are given in Table 8.

Table 8
Parameters of the potential along the pseudorotational path according to different models and methods

Parameter	Empirical		Computational (this work)	
	Baron and Harris	This work	B3LYP	MP2
B_p (cm^{-1})	3.99	3.99	—	—
V_2 (cm^{-1})	10.2	15.3	−10.2	−85.55
V_4 (cm^{-1})	−40	−31.9	−23.78	−24.59
V_6 (cm^{-1})	—	—	7.16	11.83
V_8 (cm^{-1})	—	—	−3.46	−4.14
ϕ_g (°)	43	41	56	66

very similar in shape and differ only in the vertical offset (G^0). The agreement with the experimentally observed dependence is not as good as in case of THF, which may result from the closer spacing between the lowest four PR levels and the more complex pattern of interaction between PR states.

5. Conclusion

In the present work, we have observed and analyzed the rotational structure of the three hindered PR bands in 1,3-dioxolane, two of which, $n = 2 \rightarrow 3$ and $n = 0 \rightarrow 3$ were not observed previously, and thereby established the energies of the four lowest pseudorotational states. The analysis of the totality of the avail-

able data from FIR [11] and microwave [32] experiments allowed us to refine the parameters of the PES for hindered pseudorotation in DOX. The empirical surface shows 4 equivalent minima at asymmetric configurations and two pairs of equivalent maxima at symmetric C_2 and C_s configurations, with the former configuration being higher in energy. Quantum chemistry calculations, particularly the B3LYP method, produced a similar, but not identical PES, and results qualitatively corresponding to the observed rotational constants. The study of the DOX molecule using the previously developed analytical and computational formalism [14], showed that the variation of the rotational constants in different PR states is fairly sensitive to the details of the PES and therefore, such an analysis is useful for the study of the details of PES in similar systems. The accuracy of the modeling and the prediction of the submillimeter wave and FIR frequencies of the PR bands could be increased by additional experimental data.

Acknowledgments

The authors would like to thank The Ohio Supercomputer Center for the opportunity to perform calculations and National Science Foundation for support of this work (Grant Nos. CHE-0211281 and CHE-9974404).

References

[1] B.A. Applegate, T.A. Barckholtz, T.A. Miller, Chem. Soc. Rev. 32 (2003) 38.
[2] B.E. Applegate, T.A. Miller, T.A. Barckholtz, J. Chem. Phys. 114 (2001) 4855.
[3] B.E. Applegate, A.J. Bezant, T.A. Miller, J. Chem. Phys. 114 (2001) 4869.
[4] B.E. Applegate, T.A. Miller, J. Chem. Phys. 117 (2002) 10654.
[5] J. Laane, J. Phys. Chem. A 104 (2000) 7715.
[6] H.L. Strauss, Annu. Rev. Phys. Chem. 34 (1983) 301.
[7] D.O. Harris, G.G. Engerholm, C.A. Tolman, A. Luntz, R.H. Kim, W.D. Gwinn, J. Chem. Phys. 50 (1969) 2438.
[8] H.M. Pickett, H.L. Strauss, J. Chem. Phys. 55 (1971) 324.
[9] J.R. Durig, D.W. Wertz, J. Chem. Phys 49 (1968) 2118.
[10] W.J. Lafferty, D.W. Robbinson, R.V. St Louis, J. Chem. Phys. 42 (1965) 2915.
[11] J.A. Greenhouse, H.L. Strauss, J. Chem. Phys. 50 (1969) 124.
[12] R. Meyer, J.C. Lopes, J.L. Alonso, S. Melandri, P.G. Favero, W. Caminati, J. Chem. Phys 111 (1999) 7871.
[13] A.H. Mamleev, L.N. Gunderova, R.V. Galeev, J. Struct. Chem. 42 (2001) 365.
[14] D.G. Melnik, S. Gopalakrishnan, T.A. Miller, F.C.D. Lucia, J. Chem. Phys. 118 (2003) 3589.
[15] T.H. Chao, J. Laane, J. Mol. Spectrosc. 70 (1978) 357.
[16] L.A. Carriera, G.J. Jiang, W.B. Person, J.N. Willis, J. Chem. Phys. 56 (1972) 1440.
[17] A.H. Mamleev, N.M. Pozdeev, Zh. Strukt. Khim. 20 (1979) 949.
[18] J.R. Durig, W.J. Lafferty, W.D. Gwinn, V.F. Kalasinsky, J. Phys. Chem. 80 (1976) 1199.
[19] L.F. Colegrove, J.C. Wells, J. Laane, J. Chem. Phys. 93 (1990) 6291.
[20] J. Laane, J. Chem. Phys. 50 (1969) 1946.
[21] R.R. Durig, J.N. Willis, J. Mol. Spectrosc. 32 (1969) 320.
[22] A.H. Mamleev, N.M. Pozdeev, N.N. Moiseeva, J. Mol. Struct. 33 (1976) 211.
[23] E.C. Thomas, V.W. Laurie, J. Chem. Phys. 51 (1969) 4327.
[24] W. Caminati, H. Oberhammer, G. Pfafferott, R.R. Filgueira, C.H. Gomez, J. Mol. Spectrosc. 106 (1984) 217.
[25] W. Caminati, A. Dell'Erba, G. Maccaferri, P.G. Favero, J. Mol. Spectrosc. 191 (1998) 45.
[26] G. Pfafferott, H. Oberhammer, J.E. Boggs, W. Caminati, J. Am. Chem. Soc. 42 (1985) 2305.
[27] C.M. Cheatham, J. Laane, J. Chem. Phys. 94 (1991) 5394.
[28] J. Choo, J. Laane, J. Chem. Phys. 101 (1994) 2772.
[29] D.W. Wertz, J. Chem. Phys. 51 (1969) 2133.
[30] S.J. Leibowitz, J. Laane, R. Verastegui, J.R. Villarreal, J. Chem. Phys. 96 (1992) 7298.
[31] W.H. Green, A.B. Harvey, J.A. Greenhouse, J. Chem. Phys. 54 (1971) 850.
[32] P.A. Baron, D.O. Harris, J. Mol. Spectrosc. 49 (1974) 70.
[33] D.G. Melnik, S. Gopalakrishnan, T.A. Miller, S.P. Belov, F.C.D. Lucia, J. Chem. Phys. 114 (2001) 6100.
[34] T. Ikeda, R.C. Lord Jr., T. Ueda, J. Chem. Phys. 56 (1972) 1434.
[35] D. Melnik, Ph.D. Thesis, The Ohio State University, 2003.
[36] F.D. Lucia, R.L. Cook, P. Helminger, W. Gordy, J. Chem. Phys. 55 (1971) 5334.
[37] H.M. Pickett, J. Mol. Spectrosc. 148 (1991) 371.